

# Design and Testing of a Heavy-Duty Platform for Autonomous Navigation in Kiwifruit Orchards

Mark Hedley Jones<sup>a,\*</sup>, Jamie Bell<sup>b,\*\*</sup>, Daniel Dredge<sup>a</sup>, Matthew Seabright<sup>a</sup>,  
Alistair Scarfe<sup>c</sup>, Mike Duke<sup>a</sup>, Bruce MacDonald<sup>b</sup>

<sup>a</sup>*School of Engineering, University of Waikato, Hamilton, New Zealand*

<sup>b</sup>*Faculty of Engineering, University of Auckland, Auckland, New Zealand*

<sup>c</sup>*Robotics Plus Ltd, Neunham Innovation Park, Tauranga, New Zealand*

---

## Abstract

Horticultural robots designed for in-field use usually require a means of transportation around orchards or farms. A common approach is to directly integrate a drive system – at the expense of increasing overall complexity. Alternatively, robots can be modularised and attached to general purpose platforms. General purpose platforms reported previously are designed to carry relatively light payloads orientated toward ground based crops. This paper presents a heavy-duty platform, capable of carrying modules of up to 1000 kg, beneath 1.4 m high pergola-style kiwifruit canopies. We discuss the design of the vehicle’s software, electrical system, and mechanical structure. Sensors suitable for autonomous navigation are evaluated in-orchard and tested with prototype algorithms. Row following trials show a repeatability of within  $\pm 75$  mm using only a multi-layer lidar. With a method of automatically turning between rows, the vehicle traversed over 10 km of orchard rows unassisted.

*Keywords:* Agricultural automation, autonomous navigation, sensor selection

---

## <sup>1</sup> 1. Introduction

- <sup>2</sup> Short-term labour requirements within New Zealand’s kiwifruit industry  
<sup>3</sup> peak twice a year corresponding with the pollination and harvesting of kiwi-

---

\*markhedleyjones@gmail.com

\*\*jamie977@gmail.com

## Nomenclature

$\alpha$	Slope angle (deg)
$\Delta v$	Change in velocity ( $\text{m s}^{-1}$ )
$\omega$	Angular velocity ( $\text{rad s}^{-1}$ )
$\tau$	Torque (N m)
$B$	Nominal tyre width (m)
$C_{rr}$	Rolling resistance coefficient (unitless)
$E$	Offset between a tyre and its axis of rotation (m)
$F_{accel}$	Force required to accelerate (N)
$F_{grade}$	Force due to a gradient (N)
$F_{roll}$	Force due to rolling resistance (N)
$F_{total}$	Total force (N)
$G$	Acceleration due to gravity ( $\text{m s}^{-2}$ )
$r$	Wheel radius (m)
$u$	Friction coefficient (unitless)
$W$	Weight (N)
CAN	Controller Area Network
GLONASS	A GNSS service operated by the Russian Federation
GNSS	Global Navigation Satellite System
GPS	An GNSS service operated by the United States
IMU	Inertial Measurement Unit
PSA	Pseudomonas syringae pv. actinidiae (type of bacteria)
ROS	Robot Operating System
RTK-GPS	Realtime Kinematic GPS
SLAM	Simultaneous Localisation And Mapping (name of an algorithm)

4 fruit. The majority of employment during these peaks is filled by seasonal  
5 or casual workers (Statistics New Zealand, 2015). As kiwifruit is the coun-  
6 try's largest horticultural export by value (Statistics New Zealand, 2015),  
7 effective automation in this industry will promote economic growth. Devel-  
8 opment of an automated kiwifruit harvester with integrated drive system has  
9 previously been published (Scarfe, 2012). That work presented a platform  
10 designed to autonomously navigate though pergola-style kiwifruit orchards  
11 and had four integrated harvesting arms. Work presented here focuses on  
12 creating a platform that operates independently from orchard related tasks,  
13 such as fruit harvesting and pollination. Utilisation of a generalised base  
14 platform is increased by using it during harvesting *and* pollination seasons.  
15 Details of modules developed for use on the vehicle have been published sep-  
16 arately (Williams et al., 2019b,c,a). Those modules have been built as part  
17 of a larger project focusing on automation in kiwifruit orchards.

18 Automated kiwifruit harvesting and pollination modules incorporate com-  
19 puter controlled manipulators and real-time machine-vision systems utilising  
20 computationally expensive neural-network based image processing. As a re-  
21 sult, these systems are bulky and have geometric requirements dictated by  
22 sensors and the pergola-style growing system. They share the need for elec-  
23 trical power, air pressure, and a means of locomotion. However, they differ  
24 in the way they move when operating. The pollinating module moves at a  
25 fixed speed with minimum changes in angle, whereas the harvesting module  
26 advances a set distance between periods of being stationary. The platform  
27 must be able to self-drive in a way appropriate for each case.

28 While publishing details of BoniRob, a general purpose robotics platform  
29 for field use, the authors stated that “since the robot development already  
30 includes a high complexity, the application itself should be of comparably low  
31 complexity” (Ruckelshausen et al., 2009). By separating the development  
32 of the platform from other task-specific modules, the risk of a single part  
33 becoming overly complex is reduced.

34 The development of autonomous vehicles in agriculture is not new, but  
35 much of the literature relates to manned vehicles converted to drive-by-wire.  
36 Because the canopy of a pergola-style kiwifruit orchard can droop as low as  
37 1.4 m to the ground under fruit loading, most standard vehicles are not suited  
38 to this environment. Many autonomous vehicles designed for use in orchards,  
39 such as vineyards, rely on Global Navigation Satellite Systems (GNSS) for  
40 guidance. However, the dense foliage of a kiwifruit canopy and the surround-  
41 ing shelter-belts make receiving GNSS signals unreliable at best. Therefore,

- 42 the required vehicle must navigate through kiwifruit orchards whilst relying  
43 only on perception-based sensors. Additional requirements are to:
- 44 1. support a mass of 1000 kg,  
45 2. have a maximum height of less than 1.4 m,  
46 3. provide 8 kW of electrical power to modules,  
47 4. turn between rows using existing headland areas,  
48 5. include a bin-lifting mechanism for carrying fruit bins, and  
49 6. provide a module mounting area no more than 400 mm from the ground.



Figure 1: The presented platform driving through a pergola-style kiwifruit orchard during winter months.

50 **2. Related Work**

51 The introduction of computers and digital camera technology during the  
52 1980s sparked research into autonomous vehicles for agricultural use (Li et al.,  
53 2009). When publishing details of an autonomous vehicle in 1998, Tillett  
54 et al. cite difficulties dealing with variability in lighting and the environment  
55 as the reason no commercial vehicles were available at the time (Tillett

56 et al., 1998). Their vehicle combined wheel encoders, a compass, and ac-  
57 celerometers for odometry information. It also featured a camera based row  
58 guidance system. The system as a whole was capable of spraying individual  
59 plants whilst driving autonomously at  $0.7 \text{ m s}^{-1}$  ( $2.5 \text{ km h}^{-1}$ ). While their  
60 purpose built experimental vehicle proved capable of row following and tar-  
61 getted spraying, its design was not modular.

62 Four years later, two autonomous vehicles designed for weed mapping and  
63 control in open field crops were presented (Pedersen et al., 2002; Åstrand &  
64 Baerveldt, 2002). These platforms had simple chassis and drive systems as  
65 they were both at a prototype stage; neither were designed to carry modu-  
66 larised payloads. The first vehicle, presented by Åstrand & Baerveldt, fea-  
67 tured: two-wheel steering, two-wheel drive, a camera based row guidance  
68 system, batteries, a combustion engine, and an air-compressor. While its  
69 appearance was basic, it contained most of the functionality required by  
70 our modularised fruit harvesting and pollination modules. The second unit,  
71 described by Pedersen et al., was four-wheel drive with two-wheel steering  
72 and used satellite navigation as its primary navigation input. It was battery  
73 powered only and lacked any sort of row guidance sensor or power generation  
74 unit. The authors found that row-crop based navigation using satellite navi-  
75 gation alone was not practical and proposed the integration of a row-guidance  
76 sensor in their next design. They also proposed a revised drive system with  
77 four-wheel steering.

78 Two years later, the revised design proposed by Pedersen et al. (2002)  
79 was presented by Bak & Jakobsen (2004). Its drive system was modularised  
80 with four identical drive/steering modules mounted to the chassis. This  
81 revised chassis featured a three-point suspension system, which ensured all  
82 four wheels stayed in contact with the ground. The system also incorporated  
83 the row-guidance sensor as proposed in earlier work, as well as a Real-Time  
84 Kinematic enabled GPS receiver (RTK-GPS), fibre optic gyroscope, compass,  
85 and wheel encoders. The authors noted that the control strategy for the  
86 four independently controlled wheels was “non-trivial”. While much more  
87 developed than the previous work of Pedersen et al. (2002), the platform was  
88 not designed to: carry heavy payloads, operate in the absence of satellite  
89 navigation, or power itself beyond its battery capacity.

90 In 2009, details of BoniRob were published by Ruckelshausen et al. (2009).  
91 Similar to the previous unit presented by Bak & Jakobsen (2004), it featured  
92 a gyroscope, RTK-GPS receiver, and four-wheel steering. However, it in-  
93 troduced the use of both single-plane and multi-layer laser range scanning,

94 known as lidar, for perception and row detection. A 2.8 kW petrol engine  
95 could also be mounted to the chassis, additional to its on-board batteries. It  
96 was capable of carrying a 150 kg payload in its dedicated module space. What  
97 made BoniRob particularly interesting was its ability to alter its track-width  
98 by actuating the legs to which its wheels were mounted. Like the robots be-  
99 fore it, BoniRob was designed for use on open-field crops. During the previous  
100 year, some of these authors published details of a much simpler robot named  
101 ‘Weedy’ (Klose et al., 2008), also an open-field crop based sensing platform.  
102 BoniRob represents the first of the more general-purpose platforms designed  
103 to carry modularised payloads.

104 Most recently, Bawden et al. (2017) published details of their field-crop  
105 robot – Agbot II. For locomotion it uses two driven wheels in a differential  
106 drive configuration with castor wheels for support. It is battery powered  
107 and designed to autonomously return to a shipping container with a built-in  
108 solar powered charging station. The vehicle is made of two side modules  
109 bridged by a modular ‘implement unit’ containing the robotic systems. The  
110 side modules contain the drive system, whereas the centrepiece is designed  
111 to be specific to the application. Like the previously mentioned robots, its  
112 payload capacity (200 kg) is insufficient for our tasks and is orientated toward  
113 ground-based crops.

114 Of particular relevance, is the earlier work of Scarfe et al. on an au-  
115 tonomous kiwifruit picking robot (Scarfe et al., 2009; Scarfe, 2012). That  
116 work involved the creation of a hydraulically driven platform, with two-wheel  
117 steering and four-wheel drive. Four fruit-harvesting arms and a bin-lifting  
118 mechanism were directly integrated to the vehicle’s chassis. While that plat-  
119 form was designed to navigate through kiwifruit orchards autonomously, its  
120 ability to do so was not tested due to an outbreak of *Pseudomonas syringae*  
121 *pv. actinidiae* (PSA), which closed access to kiwifruit orchards. The platform  
122 had a petrol engine and made use of camera and lidar for row-guidance. It  
123 had sufficient carrying capacity for other roles, however it lacked modularity  
124 – restricting its use to kiwifruit harvesting.

125 With the exception of the platform presented by Scarfe (2012), all of the  
126 reviewed platforms were designed for use with open-field crops. None were  
127 designed for harvesting operations and therefore were not capable of carry-  
128 ing bins. Referring back to the statement from Ruckelshausen et al. (2009)  
129 that “the application itself should be of comparably low complexity”, one  
130 can see why research thus far has focused on simpler tasks such as inspection  
131 or weeding. However, once designs move past these applications it becomes

132 necessary to accommodate other shared requirements. A fork-lift mechanism  
 133 is general enough that most orchard related tasks can benefit from it. For  
 134 example, during harvesting it can hold a fruit collection bin. During a pollin-  
 135 nation season it can hold a tank of liquid pollen solution. The ability to pick  
 136 up a standard pallet has broad applications in and around orchards too.

137 Reported use of GNSS systems indicate that they are not suitable for  
 138 navigating row based crops on their own. With regards to the use of RTK  
 139 based GNSS guidance, Slaughter et al. points out the trade-off of requiring an  
 140 “unobstructed ‘view’ of the sky from all parts of the field” (Slaughter et al.,  
 141 2008). Li et al. (2009) conclude that the use of either GPS and machine  
 142 vision, or GPS and lidar will become a development trend. Based on the  
 143 increased reception requirements, we discount the use of RTK based systems,  
 144 but still consider the use of general purpose GNSS receivers as a navigation  
 145 input.

### 146 3. Platform Design

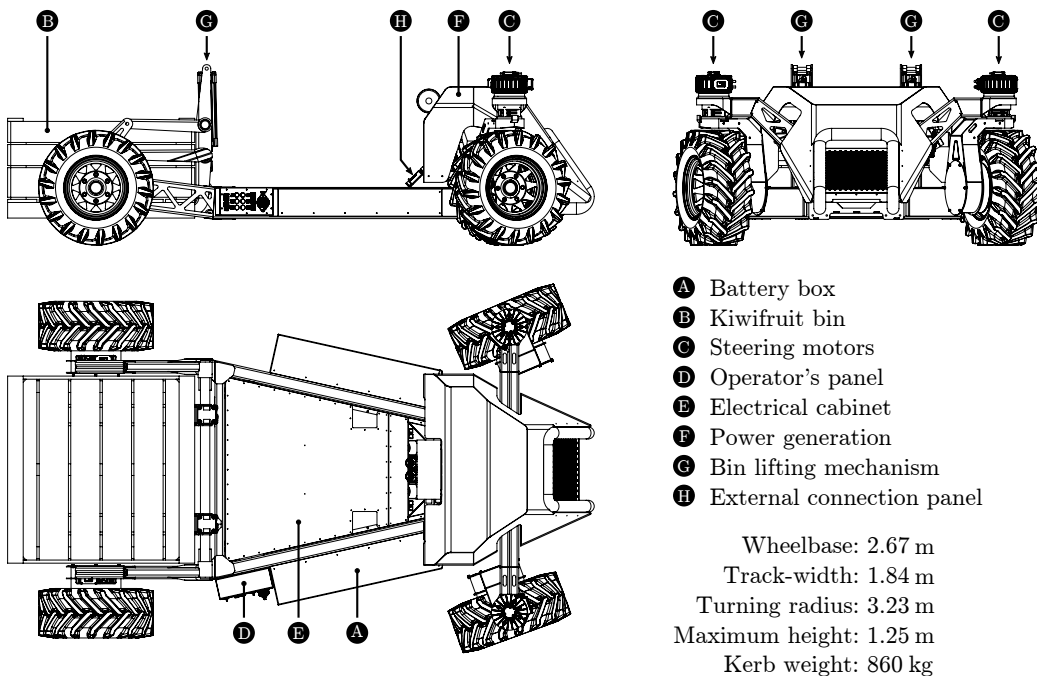


Figure 2: Profile drawings of the robotic platform with kiwifruit bin.

147 The vehicle's design is mostly influenced by the need to carry modularised  
148 robotic systems and fruit bins. Existing commercial platforms suitable for use  
149 in horticulture already exist, such as the Warthog from ClearPath Robotics,  
150 but the maximum payload, battery life, and vehicle geometry make them  
151 unsuitable for kiwifruit harvesting. The mass of robotic modules for pollin-  
152 nation or harvesting can be as much as 600 kg and a bin of kiwifruit adds  
153 an additional 400 kg. The minimum canopy height in typical commercial  
154 orchards ranges from 1.4 m to 1.7 m, so the vehicle must also have a low  
155 profile. Modules carried by the platform require clearance from the canopy  
156 in addition to the height they occupy themselves. To maximise the space  
157 available to these modules the platform must be low-slung at the point they  
158 attach. Figure 2 illustrates the platform's design, with module area allocated  
159 between markers 'G' and 'H' in the side-view (top left). The top surface of  
160 the chassis in this region sits 360 mm above the ground.

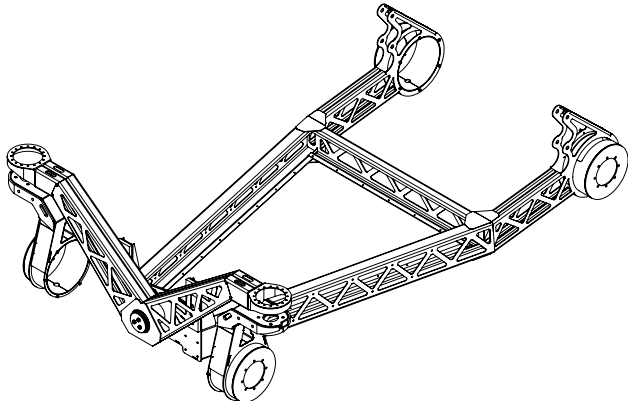


Figure 3: Drawing of the vehicle's chassis showing the front pivoting mechanism and steering linkages. The laser-cut and folded structure has a total mass of 190 kg.

161 The chassis is assembled from sections of 3 mm laser-cut and folded mild  
162 steel. The sections are welded together on jigs, also made from laser-cut  
163 and folded steel, before being powder-coated and assembled. Much of the  
164 folded chassis structure contains triangular cut-outs, reducing mass while  
165 having minimal impact on rigidity. Finite element analysis was used during  
166 the design phase to help identify areas needing to be strengthened and areas  
167 where material could be removed. This helped to ensure the platform met  
168 its target load capacity of 1000 kg, while the bare chassis weighs only 190 kg.  
169 A drawing of the bare chassis is shown in Figure 3.

170 Bin lifting forks occupy the area between the rear wheels. Fuel and com-  
171 pressed air tanks sit over the right-hand rear wheel, which can be seen in  
172 Figure 1. The bin lifter is actuated by two vertically mounted double-acting  
173 pneumatic cylinders (SMC CP96D100-320) which are controlled by a pneu-  
174 matic valve block. Each cylinder is capable of exerting 4700 N at 600 kPa or  
175 6300 N at 800 kPa.

176 *3.1. Steering*

177 The steering geometry is Ackermann based, with the front two wheels  
178 being actuated by brushless AC motors (Heinzmann PSM-G100). These  
179 motors can generate 7.32 N m of torque with a maximum angular velocity of  
180 3000 rev/min and are rated at 2.3 kW. Their outputs are fed through fixed-  
181 ratio planetary gearboxes with a 64:1 reduction, increasing torque to 470 N m  
182 while reducing the maximum angular velocity to 47 rev/min.

183 Torque requirements for the steering motors are based on a static friction  
184 scenario with the vehicle loaded with a 1000 kg mass while sitting on concrete.  
185 This is described by the following equation:

$$\tau = Wu\sqrt{\frac{B^2}{8} + E^2} \quad (1)$$

186 where  $\tau$  is the torque required to break static friction,  $W$  is the weight  
187 transmitted through each wheel,  $u$  is the coefficient of friction,  $B$  is the  
188 nominal width of the tyre, and  $E$  is the offset between the tyre's contact  
189 surface and its axis of rotation. The axis of rotation on the vehicle lies  
190 directly through the centre of the tyre, meaning  $E = 0$ . A value of 0.75 was  
191 used as the coefficient of friction as a best-guess representation of a tractor-  
192 grip tyre on dry concrete. The mass of the vehicle (800 kg), plus payload  
193 (1000 kg), and fuel (60 kg) adds to 1860 kg. Allowing for uneven weight  
194 distribution and a safety margin, the per-wheel mass supported is 500 kg, or  
195 a weight of 4900 N. The tyre width is 0.28 m. By combining these values, as  
196 per Equation 1, a torque of 388 N m is required to overcome static friction  
197 when actuating the steering wheels.

198 Actuating the steering wheels independently removes the need for me-  
199 chanical linkages between them, allowing for more extreme steering angles  
200 and a simpler mechanical design. Both steered wheels have the freedom to  
201 rotate 330°, artificially limited by mechanical stops. At the tightest steering  
202 angle of 90°, the centre-point of the turn is located at the midpoint of the

203 rear wheels. The turning radius in this case should be equal to the distance  
204 between the front bumper and the rear wheels (3.18 m).

205 Implementing a four-wheel steering system would shift the pivot point to  
206 the vehicle's centre, roughly halving the turn radius, but this was deemed un-  
207 necessary. Headlands in kiwifruit orchards are sized for tractors with much  
208 larger turning radii than that of our platform. The use of a two-wheeled  
209 steering system removes the need to develop the "non-trivial" control strate-  
210 gies required by Bak & Jakobsen (2004). It also increases the usable area at  
211 the rear of the vehicle by removing the need for clearances around actuated  
212 wheels. A skid steer system was expected to cause ground damage to a level  
213 considered unacceptable to orchard owners.

214 The steering motors have incremental encoders, but no means of absolute  
215 positioning built-in. This means that the front-wheel angles must be aligned  
216 before use. A homing sequence at boot-up is used to find an absolute angle as  
217 a reference point for incremental rotation data. Inductive proximity sensors  
218 are used to detect the position of the wheels during this sequence.

219 *3.2. Drive system*

220 The vehicle features a three-point suspension system, similar to that used  
221 by Bak & Jakobsen (2004), to ensure all wheels remain in contact with the  
222 ground. It uses a pivoting front axle to do this and is depicted in Figure 3.  
223 As the operating speed for the vehicle is  $1.39 \text{ m s}^{-1}$  ( $5.0 \text{ km h}^{-1}$ ), the tyres  
224 alone were expected to provide sufficient shock absorption.

Performance requirements for the vehicle's traction system, whilst loaded,  
during up-hill acceleration, were calculated as follows:

$$F_{roll} = C_{rr} \times m \quad (2)$$

$$F_{grade} = m \times G \times \sin(\alpha) \quad (3)$$

$$F_{accel} = m \frac{\Delta v}{t} \quad (4)$$

$$F_{total} = F_{roll} + F_{grade} + F_{accel} \quad (5)$$

Where  $F_{roll}$  is the force due to rolling-resistance;  $F_{grade}$  is the grade (or incline) force; and  $F_{accel}$  is the force required for mass acceleration. A rolling-resistance coefficient ( $C_{rr}$ ) of 0.04 was chosen as it represents the case of a pneumatic tyre on medium-hard soil (Robert Bosch GmbH, 2002). Other variables used are: a vehicle mass ( $m$ ) of 1900 kg, slope angle ( $\alpha$ ) of  $20^\circ$ , velocity change ( $\Delta v$ ) of  $2.78 \text{ m s}^{-1}$  ( $10 \text{ km h}^{-1}$ ), and an acceleration time ( $t$ ) of

6 s. Putting these values into Equations ??–5 gives a total force requirement of 7.99 kN. On a per-wheel basis this is 2.0 kN, or 729 N m when taking the wheel radius ( $r$ ) of 0.365 m into account. Required traction power ( $P$ ) is then calculated as follows:

$$\omega = 2\pi \times \frac{v}{2\pi r} = \frac{v}{r} \quad (6)$$

$$P = \tau\omega \quad (7)$$

where  $\omega$  is the angular velocity of a wheel,  $v$  is the vehicle velocity, and  $\tau$  is torque. At a velocity of  $2.78 \text{ m s}^{-1}$  ( $10 \text{ km h}^{-1}$ ), the calculations give a power requirement of 5.55 kW per wheel.

The selected motors are hub-mounted permanent-magnet brushless AC motors with integrated 40:1 fixed-radio planetary gearboxes (Heinzmann PSM-G120). Each motor is rated for 6.4 kW at 96 V with a maximum angular velocity of 3000 rev/min and torque of 20.4 N m. At the output of the gearbox the torque jumps to 816 N m while the angular velocity drops to 75 rev/min; giving the platform a top speed of  $2.86 \text{ m s}^{-1}$  ( $10.3 \text{ km h}^{-1}$ ).

In total there are seven brushless AC motors on the platform: four drive motors, two steering motors, and a motor used for electrical power generation. Each are connected to individual controllers (Sevcon Gen4 DC Size 4). These controllers are available in four input voltage options: 24-36V, 36-48V, 72V-80V, and 96V-110V. The six motors used for traction and steering are together capable of consuming 30.2 kW. With a 48 VDC bus this would equate to a current draw of 630 A. As 24 m of cabling is required to connect the motors and controllers to a common point on the vehicle, a 96 VDC bus was used to reduce the required gauge of that cable.

### 3.3. Power Distribution

The system's electrical bus connects the batteries and generator to motor controllers and on-board power converters. A series of heavy-duty contactors (TE Connectivity Kilovac LEV200) control each device's connection to the bus, as well as the bus's connection to the power source. Figure 4 illustrates the power-distribution on the platform.

Two battery modules attached to the sides of the chassis each house fifteen lithium-iron-phosphate (LiFePO<sub>4</sub>) batteries connected in series. Together, the batteries (Winston/Thundersky WB-LYP90AHA) provide a nominal bus voltage of 96 V and a total electrical capacity of 8.64 kWh. The battery packs were manually ‘bottom-balanced’ before being installed and

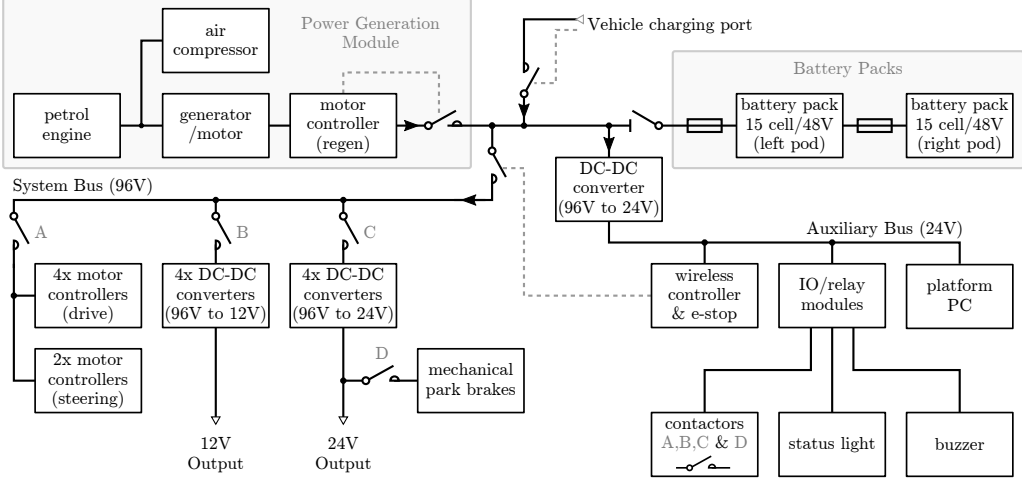


Figure 4: Power distribution system diagram. Dashed lines in grey indicate control lines to contactors.

no cell-level voltage monitoring is present. Maximum and minimum pack voltages were established by monitoring individual cells during charging and discharging. At the point that any individual cell exceeded a safe maximum/minimum threshold, the respective maximum/minimum pack voltage was recorded.

A hermetically sealed disconnect switch (Gigavac HBD41) isolates the batteries from the rest of the system. Once closed, an auxiliary 24 V bus becomes active that powers components required to bring the rest of the system on-line.

A power generation unit, comprised of a petrol engine (Honda GX-690), air compressor (Rotorcomp NK-1), and electrical generator, is housed at the front of the vehicle. Drive shafts of these units are connected via pulleys and a heavy-duty timing belt. The engine, compressor, and alternator are controlled and monitored by a micro-controller based control board. This board connects to the Platform PC via the system CAN-bus. The engine is capable of producing 16 kW, where up to 9.6 kW is converted to electrical power (limited in software) and 4.0 kW is converted to pneumatic power. The system maintains a pneumatic tank pressure of between 600 kPa and 800 kPa.

Electrical generation is done by a brushless AC motor/generator (Heinzmann PMSG-150) connected to the same model of motor controller used in

275 the drive system. The motor is a larger variant of those used for traction  
 276 and steering, minus the gearbox. Its controller is configured only to have  
 277 regenerative braking functionality, i.e., power could not be applied to the  
 278 motor. This configuration allowed the system to control the rate of power  
 279 generation by commanding brake-effort via its CAN interface. The controller  
 280 provides voltage and current limits as well as the ability to reduce output as  
 281 the batteries become charged. These settings provide all the functionality of  
 282 a general purpose battery charger, making this a cost effective and versatile  
 283 charging solution. Electrical energy from the power generation unit is fed to  
 284 the batteries in a series-hybrid configuration. An charge plug has been fitted  
 285 to allow charging of the batteries from an external source.

286 A fuel tank is fitted over the rear right-hand wheel (visible in Figure 1).  
 287 It can hold 60l of petrol, allowing the vehicle to operate continuously for  
 288 over 24 h. On-board DC-DC converters deliver 2.8 kW at 12 VDC, 3.8 kW  
 289 at 24 VDC, and 3.5 kW at 240 VAC, simultaneously. A connection panel  
 290 at the front of the module mounting area houses the weather-sealed plugs  
 291 (Anderson SPEC PAC Series) through which these outputs are accessed.

### 292 3.4. Communications Architecture

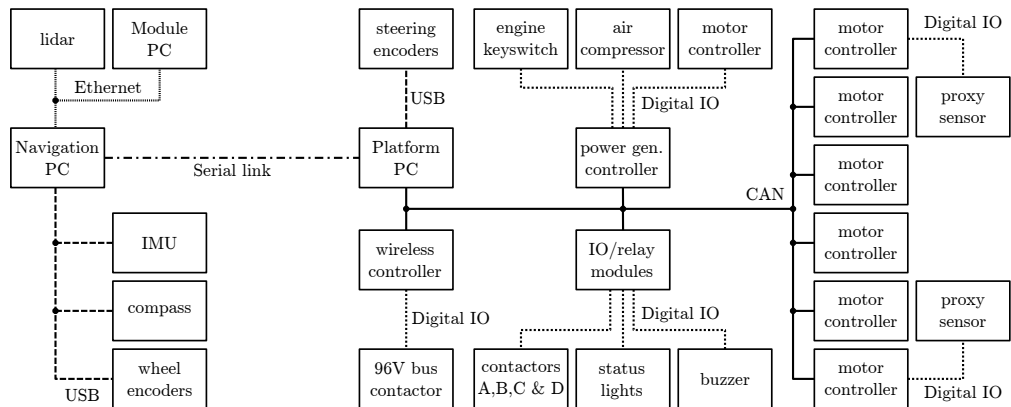


Figure 5: Communications level system diagram. Devices on right-hand side of the serial link are mechanically integrated into the vehicle, whereas those on the left are modular and can be removed.

293 The platform is centrally controlled by a general-purpose small-form-  
 294 factor PC (Intel NUC) running Ubuntu 16.04 server edition, referred to as

295 the “Platform PC”. This computer communicates with most sub-systems via  
296 a CAN bus interfaced using a USB adaptor (IXXAT USB-to-CANV2).

297 A second computer, known as the “Navigation PC”, is responsible for  
298 higher level control of the vehicle. It is used to connect to navigation sensors,  
299 send drive commands to the platform, and perform processing tasks relevant  
300 to autonomous navigation. It too is a general-purpose PC running Ubuntu,  
301 but also contains two discrete graphics cards (Nvidia GTX 1080Ti). These  
302 graphics cards were used to accelerate neural network algorithms and some  
303 image processing functions. An Ethernet network connects this PC to the  
304 mounted payload modules, while a RS422 serial link is used to communicate  
305 with the Platform PC. Figure 5 illustrates this arrangement.

306 In addition to the drive commands generated by the Navigation PC, a  
307 wireless controller (HBC Radiomatic Eco) lets the operator issue drive com-  
308 mands via joystick. The controller’s receiver module contains relays that are  
309 directly controllable from the remote control. All inputs from this controller  
310 are also broadcast onto the CAN bus and read by software nodes on the Plat-  
311 form PC. The remote control has two joystick inputs, two selector switches,  
312 four buttons, and an emergency stop switch. The emergency stop switch is  
313 connected to the 96 V bus contactor via relay outputs from the receiver unit.  
314 If this switch is closed during operation, or the controller goes out of range,  
315 power to the bus is cut within 500 ms. This engages the mechanical park  
316 brakes, removes all tractive effort from the motors, and de-powers mounted  
317 modules.

318 The open-source Robotic Operating System (ROS) is used to facilitate  
319 communication between computers and software nodes running within each  
320 computer (Quigley et al. (2009)). Nodes written using this framework fol-  
321 low either a publish-subscribe or service-client pattern. To maximise code  
322 reusability, each device on the platform has its own ROS node dedicated to  
323 publishing device data or subscribing to generated device commands. Inter-  
324 face adapters, motor controllers, wireless controllers, lidar, and encoders are  
325 examples of devices on the platform with dedicated interface nodes. Nodes  
326 can be written in either C++ or Python and can be used simply to transform  
327 or perform calculations on data while passing it between other nodes. For  
328 instance, as shown in Figure 6, an ‘Ackermann kinematics’ node transforms  
329 a steering vector into individual wheel velocity and position/angle outputs.  
330 Among other things, ROS offers the ability to monitor and record all com-  
331 munication passing through it which can be replayed and examined later.

332 The manufacturer’s configuration of the motor controllers required them

333 to be interfaced using a combination of analogue and digital inputs. For ex-  
334 ample, the accelerator and steering inputs were required to be controlled by  
335 potentiometers actuated by the vehicle's driver. However, the controllers also  
336 provide an option for a multi-motor vehicle configuration. In this configura-  
337 tion, the analogue inputs fed into a master controller are relayed to a second  
338 (slave) controller over a CAN interface. This interface is configured using a  
339 proprietary tool and is not intended for use other than between controllers  
340 configured with their software. However, by observing the communication  
341 protocol between a master and slave in operation, it was possible to imple-  
342 ment a master node in software that runs on the Platform PC. With this,  
343 all motor controllers on the platform are programmed as slave devices. This  
344 allows them to accept drive commands via a CAN interface, allowing them  
345 to be directly controlled by ROS nodes.

346 Relay modules allow the Platform PC to toggle power to on-board power  
347 supplies, motor controllers, park-brakes, and lights. They also monitor the  
348 timing of synchronisation messages transmitted by the Platform PC onto  
349 the CAN bus. These synchronisation messages are configured to occur every  
350 20 ms as an indication that the system is running as expected. Once a relay  
351 module detects an absence of these messages for 100 ms or longer it enters an  
352 error state. This causes the motor controllers and on-board power supplies  
353 to be shut-off and the park-brakes to be engaged. Synchronisation message  
354 monitoring is used as a fail-safe mechanism to ensure the system is promptly  
355 shut-down if the Platform PC fails.

356 The open-source simulation package Gazebo was used to simulate the  
357 vehicle's steering geometry with input from a game-pad. This revealed is-  
358 sues that were resolved before implementation on the physical hardware. It  
359 also provided the opportunity to tune control parameters, such as steering  
360 sensitivity, while reducing the time to test.

#### 361 **4. Qualitative Navigation Sensor Evaluation**

362 The choice of sensors incorporated into a vehicle determines which algo-  
363 rithmic approaches are available for navigation. Lidar, cameras, and GNSS  
364 receivers have been considered. Each sensor's ability to capture relevant data  
365 is evaluated qualitatively by in-orchard trials.

366 Other sensors considered for inclusion are outlined in Table 1 along with  
367 their associated issues. Factors considered were the strengths and weaknesses  
368 in the context of orchard use, reported usage in literature, and availability

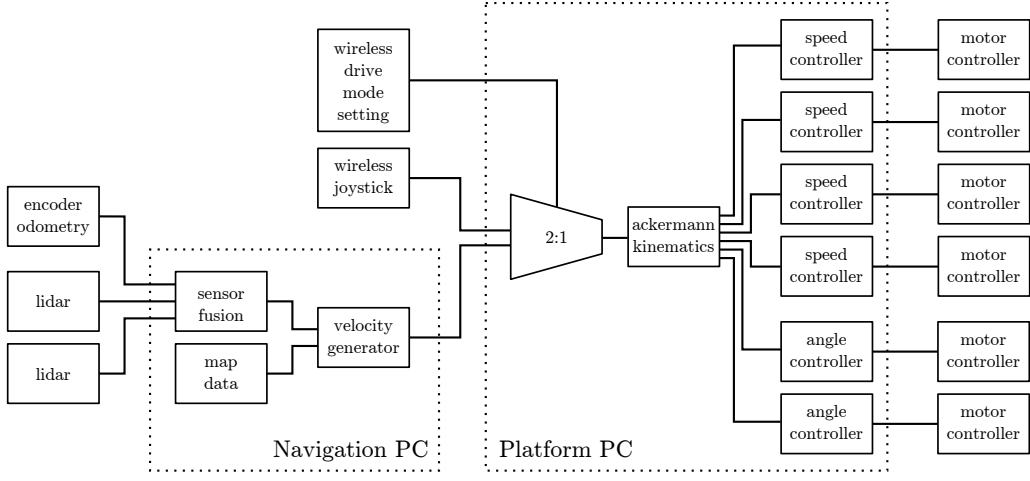


Figure 6: Simplified diagram showing connectivity between ROS nodes used for manual and autonomous platform control.

369 at a suitable price. A review of previous works highlighted both lidar and  
 370 2D cameras as offering high functionality for navigation and object detection.  
 371 Time-of-flight cameras were a compelling option based on a cost-benefit anal-  
 372 ysis, especially if cheaper units worked outdoors in the presence of sunlight.  
 373 Because localisation is such a key function, the performance of two GNSS  
 374 receivers was also evaluated.

Sensor Type	Common Issues
GNSS receiver	Prone to signal loss from surrounding foliage
Inertial Measurement Unit	Error accumulation and thermal drift
Digital Compass	Prone to disturbance by nearby metallic structures
Encoder	Error accumulation
Lidar	Reduced visibility in fog and heavy rain
Time of Flight Camera	Reduced visibility in sunlight, fog and heavy rain
Camera	Reduced visibility in fog or direct sunlight, blurring
Thermal Camera	Reduced visibility in conditions of low thermal contrast

Table 1: Sensor types considered for inclusion on the platform.

375 As the drive motors have built-in wheel encoders, basic odometry data  
 376 was already available. Encoders on driven wheels will give false readings  
 377 if wheel slippage occurs so are not be used for odometry alone. However,  
 378 the data provided can still be used to assist with mapping, localisation, and  
 379 provide velocity feedback.

380    4.1. Camera

381    Three types of camera were tested: time-of-flight, 3D stereoscopic, and  
382    traditional 2D cameras. Smaller platforms (Clearpath Husky and Adept  
383    MobileRobots Pioneer P3-AT) were used to gather data used for evaluation.  
384    Cameras were mounted 0.8 m above the ground, roughly mid-way between  
385    the ground and the canopy, facing forward.

386    The time-of-flight camera was a Basler TOF640-20GM-850NM. It pro-  
387    vides range, intensity, and confidence data at a resolution of 640 by 480  
388    pixels. This specific model was chosen as it had previously proved useful  
389    when collecting depth data of kiwifruit canopies. During that time it had  
390    been operated under a range of lighting conditions and exhibited minimal  
391    occurrences of data loss. In those conditions the camera was mounted with  
392    its principal axis aligned vertically, pointing upwards to the canopy. How-  
393    ever, subsequent testing with the camera mounted with its principal axis  
394    aligned horizontally revealed significant data loss in both sunny and overcast  
395    conditions. This is thought to be the result of two factors. The first is a  
396    lower reflectivity of objects in view of the camera when facing forwards, as  
397    opposed to facing up at a leafy canopy. The second is due to a dramatic  
398    increase in distance between the camera and the scene's subject matter. As  
399    the camera relies on active illumination of the scene, its ability to detect that  
400    illumination amongst ambient light will drop sharply with distance.

401    The 3D stereo camera tested was an Intel RealSense R200. It combines  
402    a stereo pair of infra-red cameras with a colour camera. Additionally, it  
403    features an infra-red projector as a means of adding texture to objects in its  
404    field of view to assist with stereo processing. The appealing characteristics  
405    of this sensor were its low cost and its claim of being long-range and able to  
406    work outdoors. However, in both overcast and sunny conditions it suffered  
407    from a *complete* loss of range data. This appeared to be the result of ambient  
408    light interfering with the infrared projector's signal.

409    Traditional, 2-dimensional, cameras trialled were the Basler Dart daA1600-  
410    60uc, Flir CM3-U3-13S2C-CS, and a Logitech C920 web-camera; sample im-  
411    ages are shown in Figure ???. The Logitech C920 suffered from significant  
412    motion blur that, being a consumer grade web-camera, was not surprising.  
413    It also lacked the functionality of a hardware trigger and sent images with  
414    significant latency, measured at 150 ms. The Basler and Flir cameras both  
415    produced images of sufficient quality and featured hardware triggering. The  
416    Basler camera had a USB3 interface and an average image transfer time of  
417    14 ms. The Flir camera had a USB2 interface and an average image transfer

418 time of 65 ms. The Basler offering was favoured for its later model image  
419 sensor, simpler software interface, and lower-latency.



Figure 7: Example images captured from trialled 2D cameras. Basler Dart daA1600-60uc (left), Flir CM3-U3-13S2C-CS (centre), Logitech C920 web-camera (right).

420 Both the time-of-flight and 3D stereoscopic camera systems were deemed  
421 unsuitable based on the occurrences of data loss. Images from the industrial  
422 2D cameras (from Basler and Flir) were deemed suitable for object detection  
423 and classification. This was verified by processing the data using readily  
424 accessible detection algorithms such as convolutional neural networks. Using  
425 a pair of these 2D cameras it is also possible to build a stereoscopic pair. This  
426 provides the same functionality of the 3D stereoscopic camera from Intel, but  
427 without requiring the infra-red projector. Stereo pairs of industrial cameras  
428 have since proven useful on modularised harvesting and pollination modules  
429 for localising fruit and flowers, but were not tested for row following.

#### 430 4.2. Lidar

431 Three lidar based sensors were evaluated, two single-plane and one multi-  
432 layer. The two single-plane lidar were the Hokuyo UTM-30LX and a SICK  
433 LMS111. The multi-layer lidar is a Velodyne VLP-16 which has 16 horizontal  
434 360° layers separated over 15°. Data was collected from each sensor while  
435 driving through orchard rows with the units placed 0.8 m above ground level.

436 The intention was to use lidar as a means of detecting structure defining  
437 features of the orchard, such as posts, trunks and hedges. Detecting these  
438 features should allow for row boundary detection and general mapping and  
439 localisation. However, both single-plane lidar units produced clouds of un-  
440 structured data amongst the structured features; this is shown in Figure 8.  
441 The cause was the lidar's scan plane intercepting with the above canopy  
442 whilst driving over convex terrain. Similarly, this issue arose on concave

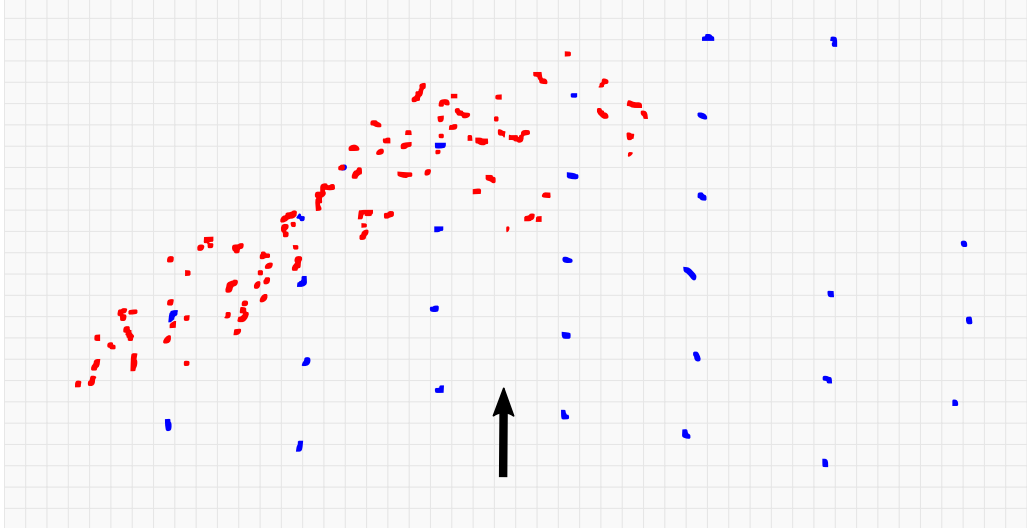


Figure 8: Birds-eye view of data captured from a single plane lidar showing non-structural points reflected by the canopy (indicated by red markers) and structural points from tree trunks and posts (blue markers). The arrow indicates the position and heading of the platform at the time of capture.

443 terrain when the plane intercepted with the ground. These situations are  
 444 depicted in Figure 9.

445 The issue was reduced by the use of a multi-layer lidar and post-processing  
 446 the scan data. Having sixteen layers available meant it was possible to select  
 447 a scan layer that gives the most useful viewing range. Referring again to  
 448 Figure 9, that would correspond to the dotted line above the horizontal  
 449 (dashed) line which intercepts with a row defining feature (a tree trunk).

450 It was decided that a multi-layer lidar would be best suited for navigation  
 451 due to its ability to see more distant features while driving on undulating  
 452 ground. A single-plane lidar could still be used at short range as an  
 453 independent channel of processing for redundancy or obstacle detection.

454 *4.3. GNSS*

455 Two GNSS receivers were evaluated: a Ublox Neo-M8N module and an  
 456 OmniSTAR 5120VBS with AX0 series antenna. Both were connected to a  
 457 single board computer (Beaglebone Black). The Ublox module was selected  
 458 for its high sensitivity and internal low-noise amplifier. It was capable of  
 459 receiving GPS, Galileo, GLONASS, and BeiDou GNSS signals concurrently.

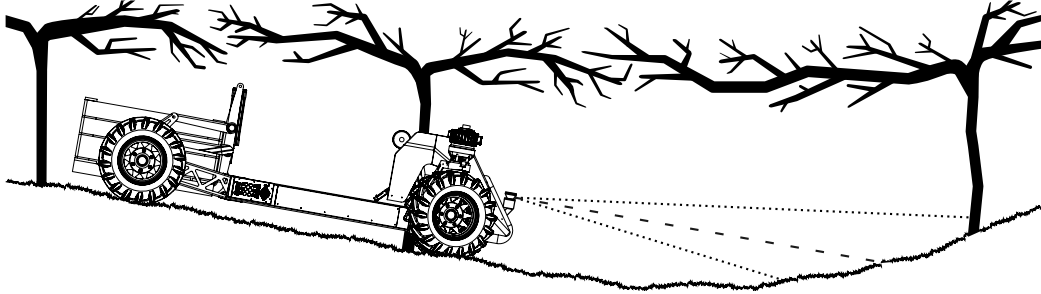


Figure 9: On concave slopes the lidar scan plane meets the ground instead of striking row-defining features. The dashed line shows a horizontal plane coming from the the lidar. Dotted lines represent the most upper and lower layers from the multi-layer lidar.

460 The OmniSTAR receiver was chosen for its external high-gain antenna (34  
 461 dB) which claims multi-path rejection. It was capable of receiving only GPS  
 462 signals.

463 The testing procedure first involved planning a path through a single row  
 464 of a kiwifruit orchard. The receivers were then tested separately over the  
 465 course of approximately two hours by walking them along the planned path.  
 466 Before testing, each unit was powered up and given 30 min to initialise in an  
 467 open area near the kiwifruit orchard. During testing, each unit was walked  
 468 slowly along the predetermined path with stops at each waypoint to provide  
 469 time for a positional fix. The path was approximately 500 m in length and  
 470 took approximately 15 min to complete, including stops at each waypoint.  
 471 Way-points were spaced at intervals of 5.5 m along the row.

472 The path followed, together with coordinates collected from the receivers,  
 473 are presented in Figure 10. It should be noted that data has been recorded for  
 474 the round-trip so represents two passes along the path. It was noticed during  
 475 testing that the signal quality lights on both receivers regularly indicated a  
 476 loss of signal.

477 The Omnistar unit appears to track the approximate path well, but the  
 478 data is sparse with regular loss of signal after entering the orchard. The Ublox  
 479 unit collected more data, but was much less accurate. It may be possible to  
 480 use a unit such as the Omnistar, which provided fewer but more accurate  
 481 readings, as a sanity check for an approximate location within orchards.  
 482 Overall, the units could not be relied on for localisation in this environment.  
 483 These results indicate that GNSS receivers with similar performance to those  
 484 trialled are unsuitable for use in kiwifruit orchards.

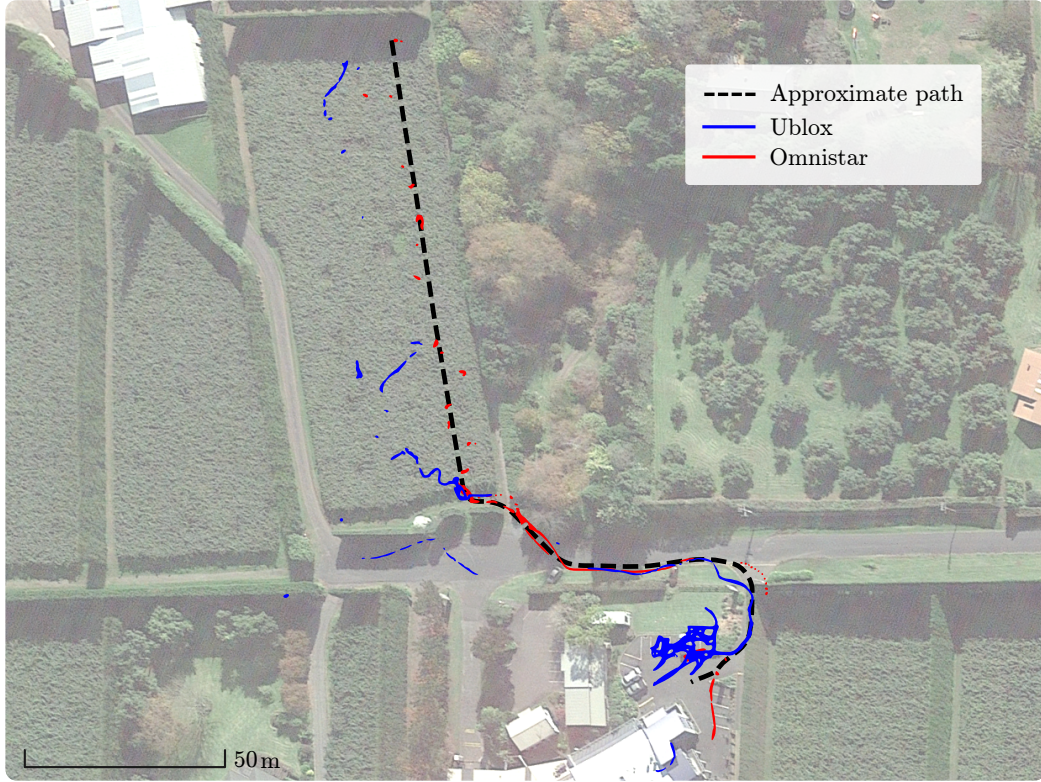


Figure 10: Aerial view of the path taken through the test orchard and the captured GPS data. Dashes, representing the approximate path, are spaced at intervals of 5.5 m.

## 485 5. Autonomous Block Traversal

486 Initially, two row following strategies were developed for block traversal.  
 487 Details and results of each have been published separately. One method used  
 488 a multi-layer lidar to detect the posts and trunks of the orchard and follow  
 489 a centre-line between them (Bell et al., 2016). This involved segmenting  
 490 points related to posts/trunks and then linking them together using a nearest  
 491 neighbour approach. Because posts/trunks in the same row-line are nearer  
 492 than those of the adjacent row, this approach resulted in the generation row  
 493 boundary lines. Once each side of the row was determined, linear and angular  
 494 offsets were calculated between the row's centre and the vehicle's pivot axis.  
 495 Those offsets were then used to steer the vehicle so as to maintain the desired  
 496 heading.

497 The second method used a single camera combined with a convolutional

498 neural network to segment areas within the captured image stream (Bell  
499 et al., 2017). These segmented areas were: traversable space, tree-lines, and  
500 row-ends. The area of the image marked as traversable space was used to  
501 calculate a centreline based on the area’s pixel-width in the image. That  
502 centreline was then used to generate a control vector to keep the vehicle  
503 centred with respect to the traversable area.

504 Both algorithms were developed on smaller, commercially available, plat-  
505 forms while the presented platform was being fabricated. A laptop (Dell  
506 E6410) with integrated graphics processor (Nvidia M5000M) was used on  
507 those test platforms to process sensor data and generate drive vectors. Both  
508 approaches produced paths that led to reproducible row following behaviour.

509 To determine when the vehicle was at the end of a row, the multi-layer  
510 lidar was used to detect the absence of canopy in a volume above the front  
511 and to the sides of the vehicle. The camera based method was unable to  
512 detect this end-of-row condition which is necessary for initiating the turn.  
513 It also lacked the ability to locate obstacles, which is critical for our target  
514 platform due to its size and power. Also, the lidar based approach required  
515 much less computational power to achieve similar performance. While it  
516 would be possible to combine the approaches, only the lidar based method  
517 was adapted for use on the target platform.

518 The multi-layer lidar was mounted horizontally above the front-right  
519 steering motor, visible in Figure 1 and in Figure 12. The smaller platforms  
520 used a skid-steer geometry, whereas our platform uses Ackermann steering  
521 geometry. When turning, a skid drive platform pivots along a lateral axis  
522 passing midway between the front and rear wheels. On the target platform  
523 however, that axis is aligned along what would be the rear axle. The software  
524 was modified to account for the change in pivoting axis as well as the new  
525 mounting location for the lidar.

526 Figure 11 presents a state diagram illustrating the steps taken when au-  
527 tonomously traversing an orchard block. The multi-layer lidar is used to  
528 detect whether the vehicle is *in\_row* or *out\_of\_row* based on the detected  
529 presence of canopy. A row-end turn sees the platform execute a series of  
530 turn segments which have previously been tuned for the specific row num-  
531 ber and turn direction. To start with, a template set of turn-segments is  
532 executed at each row’s end while under observation. If the vehicle gets too  
533 close to obstacles or nearby boundaries during execution, the operator would  
534 intervene before collision occurs.

535 A complete row-end turn can contain any number of ‘turn segments’. A

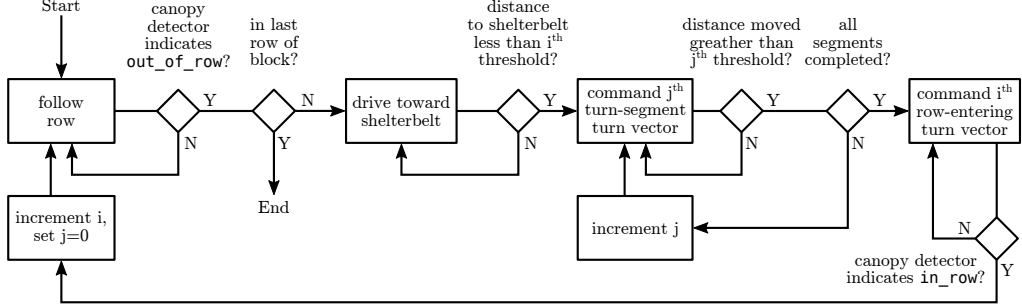


Figure 11: Flow-chart of the developed autonomous block traversal algorithm.

‘turn segment’ is simply a vector and an end-condition. Once the operator intervenes, he/she will tweak relevant parameters of the turn. This can be widening or tightening as well as lengthening or shortening the distance or angle of each segment. Finally, if an object is detected in the vehicle’s path during a turn, the steering angle is automatically increased so as to avoid the object, or the vehicle stops if the object is unavoidable. This happens independently from the parameters contained in the map. Figure 12 shows the platform performing a row-end turn while under autonomous control.

#### 544 5.1. Pure Row-following

545 A third row-following algorithm was developed which was based on Bell  
546 et al. (2016), but with three key differences. The first was that the algorithm  
547 made no attempt to turn between rows or avoid obstacles; it simply followed  
548 a row until it detected the row’s end.

549 Secondly, point-cloud data was filtered based on each point’s height above  
550 the ground. This involved first filtering out points that were expected to rep-  
551 resent the ground and using them to generate a representative 3D-surface.  
552 That surface was then used to filter the remaining points based on their  
553 height above the surface/ground; not so far as to potentially be part of the  
554 overhead canopy, but not so close that they may be weeds or related to the  
555 ground itself. Further processing checked the geometric relationship of the  
556 remaining points and made predictions about the location of posts/trunks.  
557 The process involved evaluating groupings of four posts/trunks to find those  
558 likely to represent adjacent pairs on either side of the row – forming a rect-  
559 angle. These rectangles were then evaluated using a cost-function to sort  
560 for those having regular internal angles, correct orientation, and appropriate



Figure 12: A row end turn being performed autonomously by the platform. The multi-layer lidar (Velodyne VLP-16) is visible above the front-right steering motor.

561 side lengths. A similar process was then repeated to join the rectangles into  
 562 lattices, representing a continuous section of orchard row. Such an arrange-  
 563 ment can be seen in Figure 18 where a ladder-like structure is used to connect  
 564 the posts/trunks in the generated map. Again using a cost-function, each  
 565 lattice-section-proposal was evaluated based on the regularity of the areas of  
 566 the rectangles they were made up of, the lattice’s overall linearity, and the  
 567 number of rectangles it contained. The highest scoring lattice was then used  
 568 as the best interpretation of the row’s geometry. This process was repeated  
 569 for every data frame sent from the lidar (approximately 10 Hz). The final  
 570 stage located the mid-point of the furtherest post/trunk pair in front of the  
 571 vehicle, which was used as a steering target. The position of the steering tar-  
 572 get was averaged over 10 samples to both stabalise its location and smooth  
 573 its transition to a newly detected post/trunk pair.

574 The third alteration was that the detection of the *out\_of\_row* condition  
 575 was calculated based the vehicle’s proximity to the steering target. Once  
 576 the vehicle came within 2.5 m of the steering target, it was assumed that  
 577 the vehicle had reached the end of the row. The value of 2.5 m was chosen

578 based on the amount of area at the end of the rows relative to the spacing  
579 of posts/trunks within the row.

580 **6. Testing**

581 *6.1. Mass Loading*

582 Structural integrity testing was carried out by mounting a 1100 kg mass  
583 to the vehicle's module area. No deflection of the vehicle's chassis structure  
584 was evident upon application of the test mass. Deflection of 1.5 mm was  
585 measured between the front pivot and the wheel supports. Static steering  
586 tests conducted on a dry concrete surface showed no reduction in ability to  
587 turn while loaded with the test mass. Dynamic tests involved three instances  
588 of stopping during a 10° descent at a speed of 10 km h<sup>-1</sup>. During each test  
589 the vehicle came to a complete stop within 2.0 m.

590 *6.2. Drive System*

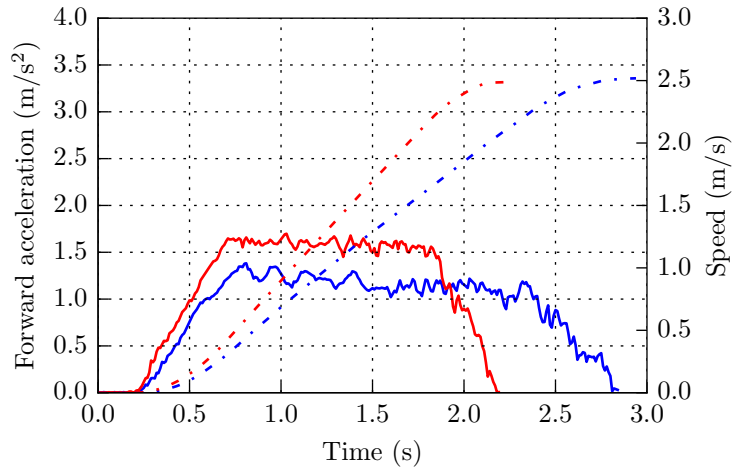


Figure 13: Acceleration of the platform on level ground (red) and up a 3.5° incline (blue).

591 Drive system testing saw the platform accelerate from a stand-still un-  
592 der manual control to its maximum speed on both level ground and whilst  
593 climbing 3.5° incline. The acceleration and inclination was measured using  
594 an Inertial Measurement Unit (IMU, LPMS-USBAL2). Figure 13 shows the

595 acceleration profile of the platform during both tests. The platform's weight  
596 during the test was estimated to have been  $(850 \pm 50)$  kg in each case.

597 In both instances the vehicle reached a top speed of  $2.5 \text{ m s}^{-1}$  ( $9.0 \text{ km h}^{-1}$ ),  
598  $0.28 \text{ m s}^{-1}$  short of the target speed. During the acceleration test on level  
599 ground, a peak power of between  $684 \text{ W}$  to  $770 \text{ W}$ , and torque of between  
600  $930 \text{ N m}$  to  $1046 \text{ N m}$  was calculated per wheel. During the inclined acceler-  
601 ation test, a peak power of between  $542 \text{ W}$  to  $610 \text{ W}$ , and torque of between  
602  $779 \text{ N m}$  to  $876 \text{ N m}$  was calculated per wheel. The torque calculations sug-  
603 gest the motors are developing their specified output of  $816 \text{ N m}$ . The mo-  
604 tor controllers are configured to supply extra torque for short bursts, which  
605 could explain why the calculated torque on level-ground is higher than this  
606 value. The incline test began with the vehicle being held stationary using  
607 torque-control, which may have affected the controller's ability to produce  
608 the higher peak torque in this case. The lower than expected top speed in  
609 both cases suggest there are configuration issues with the motor controller's  
610 speed setting.

### 611 *6.3. Turning Circle*

612 Measurements of the vehicle's turning radius were performed at speeds  
613 of  $1.39 \text{ m s}^{-1}$  ( $5.0 \text{ km h}^{-1}$ ) and  $2.78 \text{ m s}^{-1}$  ( $10.0 \text{ km h}^{-1}$ ) on both dry tarmac  
614 and damp grassland. These speeds were calculated at the mid-point between  
615 the two front wheels. Having a wheelbase of  $2.67 \text{ m}$ , these speeds equate to  
616 angular velocities of  $0.520 \text{ rad s}^{-1}$  and  $1.04 \text{ rad s}^{-1}$  respectively.

617 In each test, a line was drawn on the ground in front of the vehicle to  
618 mark its starting position. The vehicle was then turned through an angle  
619 of  $(180 \pm 10)^\circ$  under manual control with the steering angle set at  $90^\circ$ . The  
620 final angle was adjusted using odometry information to ensure the total angle  
621 was within  $(180 \pm 3)^\circ$ . A marker was then drawn on the ground at the  
622 front of the vehicle at this position. The distance between the markers was  
623 measured at  $6.45 \text{ m}$  for both surface types and both test speeds. This gives a  
624 turning radius of  $3.23 \text{ m}$ ,  $0.05 \text{ m}$  wider than the estimate based on kinematic  
625 calculations. The authors put this discrepancy down to the accuracy of the  
626 angular calibration of the front wheels.

### 627 *6.4. Bin Lifting*

628 A pallet-mounted mass of  $370 \text{ kg}$  was used to test the bin lifter. The  
629 lifter's pneumatic valve block was manually activated until the pallet sat  
630  $250 \text{ mm}$  above the ground. To raise the load, pneumatic pressure of  $800 \text{ kPa}$

631 was applied to one port of each double acting cylinder while the other port  
632 was open to atmosphere. Lowering was done by opening both ports to atmo-  
633 sphere and allowing the load to descend under its own weight. This process  
634 was repeated five times. Additionally, the vehicle was driven 300 m whilst  
635 carrying the load, including an 3.5° incline for 30 m.

636 The lifting capacity of the mechanism was sufficient to raise the load to  
637 its target height. Whilst being actuated, signs of imbalance between the two  
638 cylinders was evident which resulted in shuddering. This shuddering was  
639 caused by excessive and unbalanced static-friction between both sides of the  
640 lifter's four-bar linkage mechanism, caused from over-tight sleeve bearings.  
641 The behaviour was also evident when hand actuating the lifter. Whilst driv-  
642 ing, the load dropped by between 60 mm to 70 mm from its initial height.  
643 This drop, and the variation in resting position, is thought to be caused by  
644 the combination of static friction, driving related vibrations and the com-  
645 pression of air in the cylinders.

#### 646 *6.5. Turning Between Rows*

647 Two orchard blocks (from different orchards) were used for row-turn test-  
648 ing. These blocks will be referred to as Block A and Block B. Block A  
649 was 1.15 km in total traversable length spread over 10 rows, while Block B  
650 was 670 m in total traversable length spread over 9 rows. After tuning the  
651 row-end turning manoeuvres, our platform navigated Block A consecutively  
652 7 times without intervention. Figure 14 shows the number of interventions  
653 per traversal within Block A. A total of 19 traversals were used to tune the  
654 turns in this orchard. After tuning the row end-turns in Block B, it was nav-  
655 igated 3 times consecutively. Figure 15 shows the number of interventions  
656 per traversal whilst being tuned in Block B, with 10 traversals in total.

657 The weakness of the current navigation system is the need to tune the  
658 row-end turns manually for each site. The tuning required for the first or-  
659 chard block amounted to eight traversals of the entire block. For the second  
660 block, seven complete traversals were required for tuning. This creates a  
661 significant resource overhead for deployment to new sites. If the turns are  
662 not sufficiently tuned, two types of failure occur. The most common case is  
663 that the vehicle turns between rows too tightly or not tightly enough and  
664 the object avoidance system is not sufficiently responsive to avoid a collision.  
665 All but four interventions were due to an imminent collision with a post,  
666 resulting from this situation. Three interventions during row-end turning  
667 were due to the platform trying to recommence row following before facing

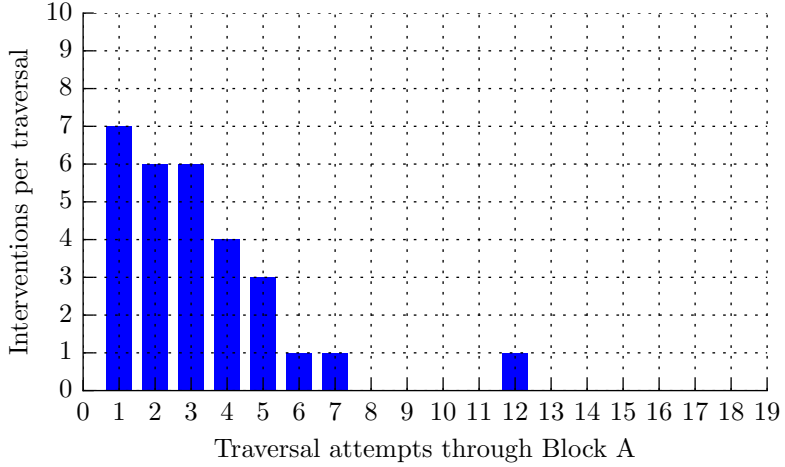


Figure 14: Number of interventions during tuning of row-end turns throughout block A.

the new target row. In this case the most feasible path for row following was detected along the headland area – instead of moving into the target row. One intervention, attempt 12 of block A, was caused by the canopy detection system triggering a row-end turn whilst still inside a row.

### 6.6. Pure Row-following

Row-following repeatability trials saw the platform self-drive through a single row, from approximately the same starting point, five times. Each trial was conducted at the vehicle’s target operating speed of  $1.39 \text{ m s}^{-1}$  ( $5 \text{ km h}^{-1}$ ). The modified version of Bell et al. (2016), as described in Section ??, was used for the row-following trial. At the beginning of each trial the navigation software was started with no prior information about the row.

To determine the vehicle’s trajectory for analysis, recordings of the lidar and IMU were taken and post-processed using a SLAM package off-line. The SLAM package used was Cartographer (version 1.0) that was integrated into a ROS package (cartographer\_ros). It was used to calculate the vehicle’s trajectory and a 2D map of the surrounding environment (Hess et al., 2016). The spacial resolution of the SLAM map was 0.05 m/pixel. Wheel odometry provided by the drive motors was not used during the trials as signs of wheel slippage were apparent. Quick measurements conducted on grass showed an imbalance in angular velocity of approximately 5 % between the rear wheels.

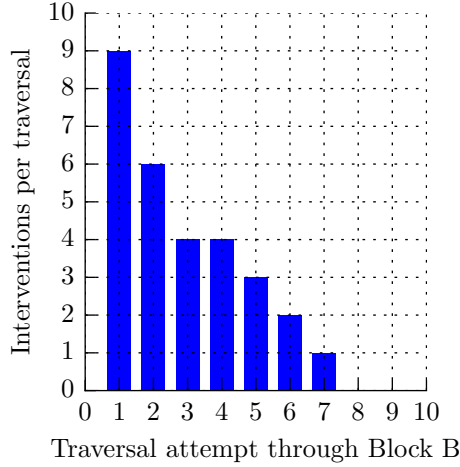


Figure 15: Number of interventions during tuning of row-end turns throughout block B.

Test number	Path length
1	106.66 m
2	103.70 m
3	104.13 m
4	104.47 m
5	104.37 m

Table 2: Total path length for each row-following test. The average length is 104.67 m and the range is 2.96 m (2.82 %).

688        The five trials and the generated SLAM map are presented together in  
 689        Figure 16. While differences in start position are estimated to be less than  
 690        0.1 m, the trajectories show a spread of 1.69 m. We attribute this to a higher  
 691        localisation uncertainty at the commencement of each trial. The total dis-  
 692        tance travelled in each trial is listed in Table 2.

693        Analysis of the tracking performance is particularly difficult as the row  
 694        itself is not linear. Figure 18 shows the same five trajectories, but has been  
 695        annotated to show approximate row boundaries. The vertical grey lines link  
 696        the post/trunk pairs used to calculate row mid-points. Calculating the mid-  
 697        point between each post/trunk-pair gives an idea of row's centre at forty  
 698        locations along the row. Due to differences in the starting and end positions  
 699        of each trial, each trajectory intersects 39 of these post/trunk-pair lines. The  
 700        distance between each of these points and the five trajectories was measured

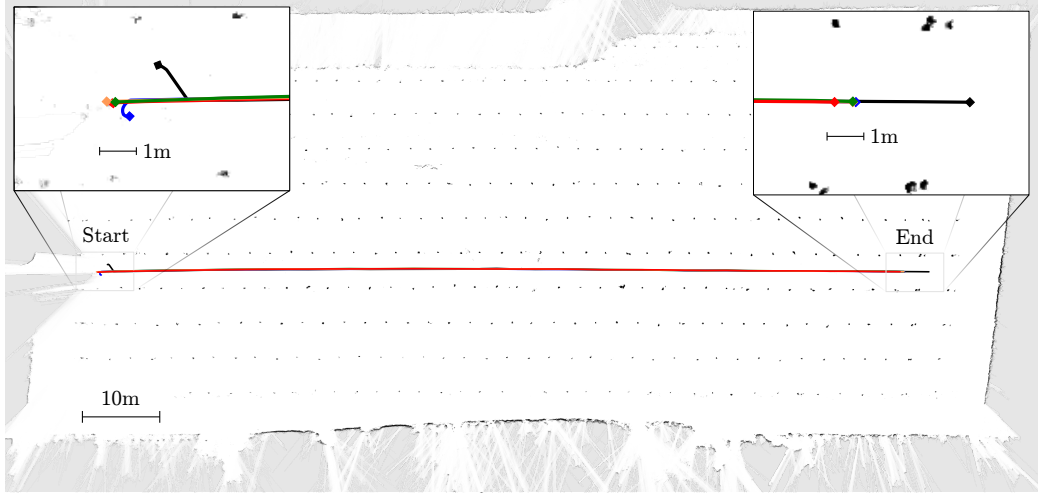


Figure 16: Trajectories recorded during five row-following repeatability trials. The trajectories are overlaid onto the generated SLAM map, which depicts the trial orchard block. Each colour represents one of five trials.

701 to quantify the deviation between each trajectory and the row's centre. Figure  
 702 presents these centreline deviations along with error estimates arising  
 703 from our measurement method. Sources of error were  $\pm 1$  pixel at each end  
 704 of the post/trunk-pair lines as well as measurement rounding errors. In this  
 705 analysis we make the assumption that the generated SLAM map was per-  
 706 fectly accurate. The maximum recorded displacement from the centreline  
 707 was 326 mm, which occurred at the twenty-second post/trunk pair.

708 Figure 19 compares each trajectory to the average trajectory. The data  
 709 presented in this figure makes no reference to the row's centre, instead each  
 710 trajectory is compared only to the average of the five trajectories. The dis-  
 711 tance between each trajectory and the average was calculated along the 39  
 712 post/trunk-pair lines shown in Figure 18. It shows that the worst case re-  
 713 peatability was less than  $\pm 75$  mm.

714 Finally, Figure 20 shows the final resting position of the vehicle after  
 715 each trial. The path-following algorithm determines the end-of-row position  
 716 based on its proximity to the heading target – placed between the furtherest  
 717 detected post/trunk pair in front of the vehicle. The end posts of each  
 718 row are spaced slightly further than is usual inside the row. That extra  
 719 spacing places the final post-pair at the boundary of the software-defined  
 720 region used to detect post/trunk pairs. Stopping slightly earlier results in

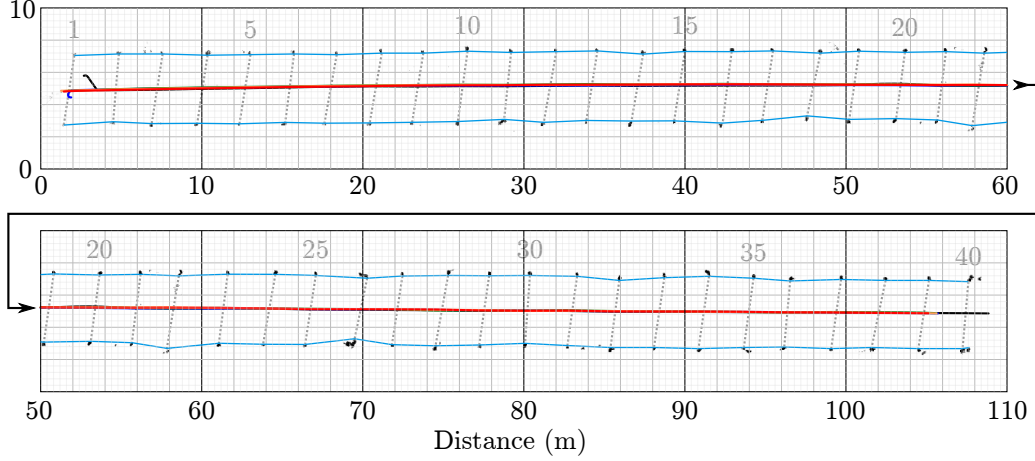


Figure 17: Cropped SLAM map with five row-following trials overlaid. Blue lines link posts and trunks along each boundary line. Grey dotted lines link post/trunk pairs, the mid-point of which define the row’s centre. Grey numbers indicate the post/trunk pair numbers relative to the start of the row.

721 the last post/trunk pair not being detected, as is the case in path groups  
 722 A and B. Additionally, there is ambiguity in the position of the second-to-  
 723 last post/trunk pair because vines have been planted in close proximity to  
 724 the posts. Analysis of the recorded sensor data suggests sensitivity to this  
 725 ambiguity to be the cause of separation between points A and B.

## 726 7. Discussion

727 The reported platform meets the requirements outlined in the introduc-  
 728 tion and has been trialled during three pollination and harvesting seasons.  
 729 However, during those operations the vehicle was mostly operated under  
 730 manual control because of the need to drive close to row boundaries. The  
 731 width of the robotic modules meant it was necessary to perform two passes  
 732 through each row in order to access the full canopy area.

733 Results from navigation tests indicate that multi-layer lidar with wheel-  
 734 encoder feedback is sufficient for row-turning tasks. The method for turning  
 735 between rows calls for further work. Row-end turning was a manual pro-  
 736 cess that involved observing pre-calculated turns and manually adjusting the  
 737 length or radius of path segments. Future work will focus on enabling the  
 738 system to plan row-end turns based on perception based sensor data without  
 739 the need for a pre-computed map. Observationally, detecting the row’s end

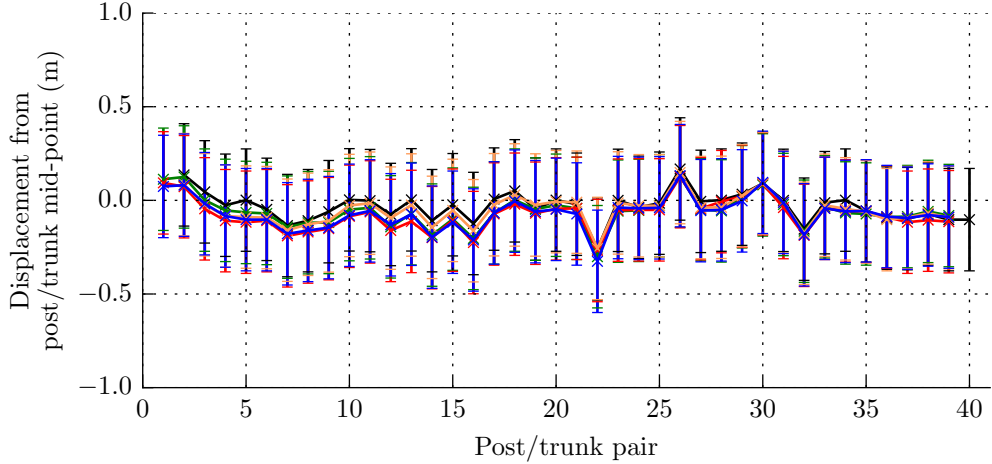


Figure 18: Vehicle displacement from calculated row centre-points during five row-following trials. Trace colours correspond to the paths presented in Figure 16. Error bars represent a  $\pm 1$  pixel error ( $\pm 0.274$  m) from the rendered SLAM map, used to calculate the row’s mid-points.

740 based on the vehicle’s proximity to the last post-pair proved more reliable  
 741 than detecting the presence/absence of canopy.

742 For pure row-following, without obstacle avoidance, a multi-layer lidar  
 743 algorithm produced paths that were repeatable to within  $\pm 75$  mm. Our  
 744 analysis showed a worst-case deviation of 326 mm from the row’s mid-point  
 745 during row-following, however this figure appears to mostly be influenced by  
 746 the non-linearity of the row itself. As Figure 17 shows, the worst case error  
 747 for each trial occurred between post/trunk pair twenty-two. Matching this  
 748 with the corresponding post/trunk pair in Figure 18 shows the placement of  
 749 the right-hand post/trunk is likely to be a contributing factor. Our method  
 750 of measuring deviation of the vehicle’s trajectory from the row’s centre calls  
 751 for improvement.

752 The structure of the pergola-style kiwifruit orchard made generating odom-  
 753 etry information directly from lidar scans reliable enough to replace wheel  
 754 encoders and IMU based odometry. This odometry source was used by the  
 755 pure-row-following algorithm presented in Section ???. It was generated by  
 756 the SLAM package (Cartographer) by matching subsequent lidar frames. As  
 757 it was based on visual information it was much less prone to drift than the  
 758 wheel encoders or IMU, although this was not quantified.

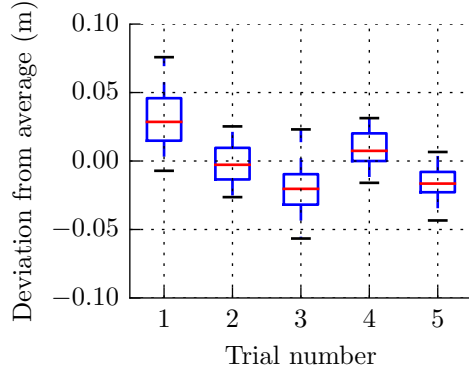


Figure 19: Repeatability analysis of the five row-following trials. Each column compares displacements of a single trajectory, from the row’s centre, to the average of the five trajectories. Whiskers represent maximum deviations in both the positive and negative directions.

759 The platform’s 96 V battery pack and electrical system introduced a elec-  
 760 trical hazard that caused delays during development, assembly, and testing.  
 761 The authors suggest a voltage of 48 V for similar developmental vehicles as  
 762 it bears a reduced risk of injury from electrical shock. Inputs of 48 V are  
 763 supported across a wider range of motors, motor controllers, and power con-  
 764 verters, but cabling requirements are increased.

765 The series-hybrid electrical configuration allowed the vehicle to drive and  
 766 provide power to subsystems without running the petrol engine. This was  
 767 useful in testing scenarios, where people are in close proximity to the vehicle,  
 768 as it eliminated exhaust fumes and reduced noise and vibration. However,  
 769 robotic modules and the bin-lifting mechanism required pneumatic pressure  
 770 to function. As the air-compressor was belt driven from the petrol engine it  
 771 was necessary to frequently run the engine. An electric air-compressor would  
 772 allow the system to run without the petrol engine for much longer periods.

773 The use of more general purpose platforms to test navigation algorithms  
 774 enabled the navigation software to be developed in parallel with the physical  
 775 hardware. Their smaller size eliminated the risk of serious injury and led to  
 776 a speed-up in development and test cycles. It also meant that navigation  
 777 testing could continue while the full sized platform was engaged in other  
 778 activities.

779 An added benefit to the modularisation of the robotic harvesting and

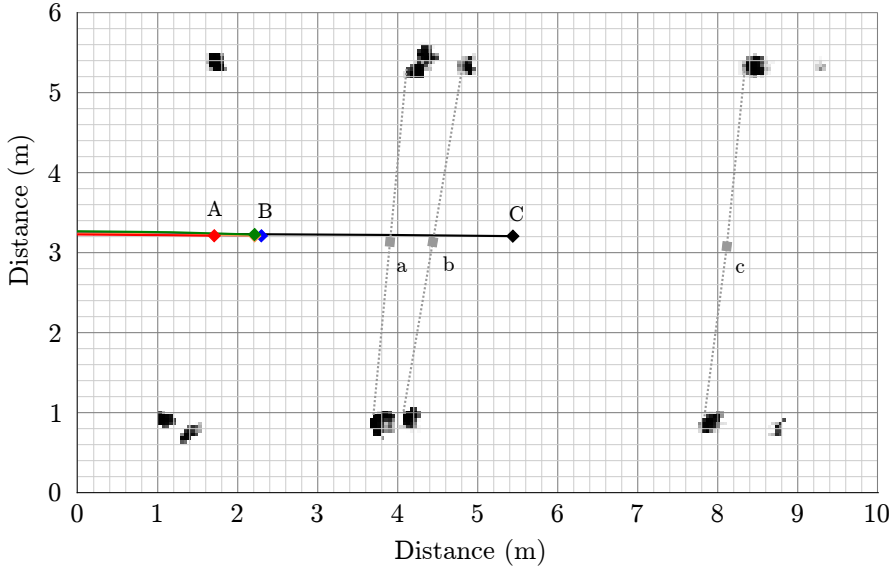


Figure 20: Graph showing row-following end positions relative to tracked row features. Grey dotted lines connect row feature pairs, with squares indicating their mid-points.

780 pollination systems was the ability to operate them independently from the  
 781 vehicle. In the event that the vehicle required repair or maintenance work  
 782 during a harvesting or pollination season, the modules could be mounted on  
 783 a trailer and towed behind a quad-bike until the vehicle returned to service.

## 784 8. Conclusion

785 We present a platform designed specifically for autonomously transport-  
 786 ing task-specific modules and kiwifruit bins through pergola-style kiwifruit  
 787 orchards. The vehicle is capable of carrying over twice the mass of simi-  
 788 lar platforms reported previously. Calculations of the drive system’s power  
 789 and torque requirements, as well as the chassis’ design, have been presented.  
 790 A four-wheel-drive system with two individually-actuated steering wheels  
 791 proved suitable for use in and around kiwifruit orchards. Subsequently, we  
 792 deem the use of a four-wheel steering configuration in this environment to  
 793 be unnecessary.

794 A variety of sensors deemed suitable for navigation were trialled in  
 795 orchard. Multi-layer lidar proved to be the most versatile sensor for orchard  
 796 based navigation owing to its wide field-of-view and robust outputs. Row

797 following trials using an algorithm based only on multi-layer lidar was repeat-  
798 able to within  $\pm 75$  mm over five trials. GNSS, time-of-flight, and infra-red  
799 stereoscopic cameras proved unsuitable as row guidance sensors. 2D cameras  
800 and neural network based processing proved capable of row following, but  
801 the lidar based method was more robust and less demanding of computation  
802 resources. Using a map of manually adjusted row-end turns, the platform  
803 has navigated over 10 km of orchard rows using only wheel-encoders and a  
804 single multi-layer lidar. A significant amount of work was required to tune  
805 the row-end-turns, which has implications for commercial deployment. Fu-  
806 ture work will focus on enabling the vehicle to plan its own row-end turns  
807 based on sensory data.

808 **Acknowledgements**

809 This research was supported by the New Zealand Ministry for Business,  
810 Innovation and Employment (MBIE) on contract UOAX1414. The authors  
811 acknowledge contributions from Phillip Ross, Gordon Neshausen, Josh Bar-  
812 nett, and Erin Simms who were involved with design and fabrication.

813 **References**

- 814 Åstrand, B., & Baerveldt, A. J. (2002). An agricultural mobile robot with  
815 vision-based perception for mechanical weed control. *Autonomous Robots*,  
816 13, 21–35.
- 817 Bak, T., & Jakobsen, H. (2004). Agricultural Robotic Platform with Four  
818 Wheel Steering for Weed Detection. *Biosystems Engineering*, 87, 125–136.
- 819 Bawden, O., Kulk, J., Russell, R., Mccool, C., English, A., Dayoub, F.,  
820 Lehnert, C., & Perez, T. (2017). Robot for weed species plant-specific  
821 management. *Journal of Field Robotics*, (pp. 1–21).
- 822 Bell, J., MacDonald, B. A., & Ahn, H. S. (2016). Row following in per-  
823 gola structured orchards. In *2016 IEEE/RSJ International Conference on*  
824 *Intelligent Robots and Systems (IROS)* (pp. 640–645).
- 825 Bell, J., Macdonald, B. A., & Ahn, H. S. (2017). Row Following in Pergola  
826 Structured Orchards by a Monocular Camera Using a Fully Convolutional  
827 Neural Network. In *Australasian Conference on Robotics and Automation*  
828 (*ACRA*) (pp. 133–140).

- 829 Hess, W., Kohler, D., Rapp, H., & Andor, D. (2016). Real-time loop closure  
830 in 2D LIDAR SLAM. In *Proceedings - IEEE International Conference on*  
831 *Robotics and Automation* (pp. 1271–1278).
- 832 Klose, R., Thiel, M., Ruckelshausen, a., & Marquering, J. (2008). Weedy  
833 – a sensor fusion based autonomous field robot for selective weed control.  
834 *Land. Technik 2008, 2045*, 167–172.
- 835 Li, M., Imou, K., Wakabayashi, K., & Yokoyama, S. (2009). Review of re-  
836 search on agricultural vehicle autonomous guidance. *International Journal*  
837 *of Agricultural and Biological Engineering, 2*, 1–16.
- 838 Pedersen, T. S., Nielsen, K. M., Andersen, P., & Nielsen, J. D. (2002). Devel-  
839 opment of an Autonomous Vehicle for Weed and Crop Registration. *Inter-*  
840 *national Conference on Agricultural Engineering AgEng2002, Budapest,*.
- 841 Quigley, M., Conley, K., Gerkey, B., Faust, J., Foote, T., Leibs, J., Wheeler,  
842 R., & Ng, A. Y. (2009). ROS: an open-source Robot Operating System.  
843 In *ICRA workshop on open source software* (p. 5). Kobe volume 3.
- 844 Robert Bosch GmbH (2002). *Electronic Automotive Handbook*. (1st ed.).
- 845 Ruckelshausen, A., Biber, P., Dorna, M., Gremmes, H., Klose, R., Linz,  
846 A., Rahe, F., Resch, R., Thiel, M., Trautz, D., Weiss, U., Doma, M., &  
847 Rahne, R. (2009). BoniRob: an autonomous field robot platform for indi-  
848 vidual plant phenotyping. *Proceedings of Joint International Agricultural*  
849 *Conference (2009), 9*, 841–847.
- 850 Scarfe, A. J. (2012). *Development of an Autonomous Kiwifruit Harvester*.  
851 Doctoral dissertation Massey University, Palmerston North, New Zealand.
- 852 Scarfe, A. J., Flemmer, R. C., Bakker, H. H., & Flemmer, C. L. (2009).  
853 Development of an autonomous kiwifruit picking robot. In *Autonomous*  
854 *Robots and Agents, 2009. ICARA 2009. 4th International Conference on*  
855 (pp. 380–384). IEEE.
- 856 Slaughter, D. C., Giles, D. K., & Downey, D. (2008). Autonomous robotic  
857 weed control systems: A review. *Computers and Electronics in Agriculture*,  
858 *61*, 63–78.

- 859 Statistics New Zealand (2015). Annual Fruit Exports Hit  
860 \$2 Billion for First Time. [http://archive.stats.govt.nz/browse\\_for\\_stats/industry\\_sectors/imports\\_and\\_exports/OverseasMerchandiseTrade\\_MRJun15-x1.aspx](http://archive.stats.govt.nz/browse_for_stats/industry_sectors/imports_and_exports/OverseasMerchandiseTrade_MRJun15-x1.aspx). Accessed: 2018/01/18.
- 863 Tillett, N. D., Hague, T., & Marchant, J. A. (1998). A Robotic System for  
864 Plant-Scale Husbandry. *Journal of Agricultural Engineering Research*, 69,  
865 169–178.
- 866 Timmins, J. (2009). Seasonal Employment Patterns in the Horticultural In-  
867 dustry. <http://archive.stats.govt.nz/~media/Statistics/browse-categories/income-work/employment-unemployment/leed/research-reports/seasonal-employment-patterns.pdf>. Accessed: 2018/01/18.
- 870 Williams, H., Jones, M. H., Nejati, M., Penhall, N., Lim, J., Seabright,  
871 M., Bell, J., Ahn, H. S., Scarfe, A., Duke, M., & MacDonald, B. (2019a).  
872 Improvements to and large-scale evaluation of a robotic kiwifruit harvester.  
873 *Journal of Field Robotics*, (pp. 1–20).
- 874 Williams, H., Nejati, M., Hussein, S., Penhall, N., Lim, J. Y., Jones, M. H.,  
875 Bell, J., Ahn, H. S., Bradley, S., Schaare, P., Martinsen, P., Alomar,  
876 M., Patel, P., Seabright, M., Duke, M., Scarfe, A., & MacDonald, B.  
877 (2019b). Autonomous Pollination of Individual Kiwifruit Flowers: Toward  
878 a Robotic Kiwifruit Pollinator. *Journal of Field Robotics*, (pp. 1–17).
- 879 Williams, H. A., Jones, M. H., Nejati, M., Seabright, M. J., Bell, J., Penhall,  
880 N. D., Barnett, J. J., Duke, M. D., Scarfe, A. J., Ahn, H. S., Lim, J. Y.,  
881 & MacDonald, B. (2019c). Robotic Kiwifruit Harvesting using Machine  
882 Vision, Convolutional Neural Networks, and Robotic Arms. *Biosystems  
Engineering*, 181, 140–156.